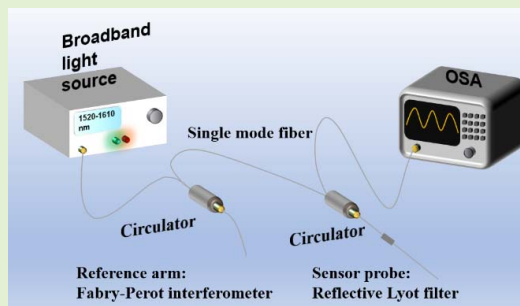


# Fiber Optic Temperature Sensor With Online Controllable Sensitivity Based on Vernier Effect

Maolin Dai<sup>1</sup>, Graduate Student Member, IEEE, Zhenmin Chen, Member, IEEE, Yuanfang Zhao, Graduate Student Member, IEEE, Xin Mu<sup>2</sup>, Xuanyi Liu, Student Member, IEEE, M. S. Aruna Gandhi<sup>3</sup>, Member, IEEE, Qian Li<sup>4</sup>, Member, IEEE, Shengzhen Lu, Shen Liu<sup>5</sup>, and H. Y. Fu<sup>6</sup>, Senior Member, IEEE

**Abstract**—A highly-sensitive temperature sensor with controllable sensitivity based on Vernier effect by cascading a tunable extrinsic Fabry-Perot interferometer (FPI) and a fixed reflective Lyot filter (RLF) is theoretically investigated and experimentally demonstrated. The temperature sensitivity can be tuned by modulating the cavity length of the extrinsic FPI and online monitoring the envelope of superimposed spectrum with optical spectrum analyzer (OSA). The FPI works as the reference arm to tune the temperature sensitivity of the sensing system, while the RLF with 1-meter polarization maintaining fiber (PMF) acts as the sensing probe. Experimental results prove that by changing the cavity length of the FPI, the sensitivities of  $-3.82 \text{ nm}/^\circ\text{C}$ ,  $-8.33 \text{ nm}/^\circ\text{C}$  and  $-14.63 \text{ nm}/^\circ\text{C}$  can be achieved. Compared with the single sensing element, the sensitivities are magnified by 3.78, 8.25 and 14.49 times. The proposed temperature sensor is feasible to be applied practically in scenarios which require different temperature sensitivities in demanded temperature detection ranges.

**Index Terms**—Optical fiber sensors, temperature sensors, Fabry-Perot interferometer, Lyot filter, Vernier effect.



## I. INTRODUCTION

TEMPERATURE monitoring is an essential calibration in several industrial fields, such as precision processing and biomedicine. Currently, the investigation of temperature sensors attracts tremendous research interests from the pho-

Manuscript received June 25, 2021; revised July 26, 2021; accepted July 26, 2021. Date of publication July 30, 2021; date of current version October 1, 2021. This work was supported in part by the Science, Technology and Innovation Commission of Shenzhen Municipality under Grant JCYJ20180507183815699, and in part by the Innovation Group Project of Southern Marine Science and Engineering Guangdong Laboratory (Zhuhai) under Grant 311021011. The associate editor coordinating the review of this article and approving it for publication was Dr. Sanket Goel. (Corresponding author: H. Y. Fu.)

Maolin Dai, Yuanfang Zhao, Xin Mu, and Xuanyi Liu are with Tsinghua Shenzhen International Graduate School and Tsinghua-Berkeley Shenzhen Institute, Tsinghua University, Shenzhen 518055, China.

Zhenmin Chen was with Tsinghua Shenzhen International Graduate School, Tsinghua University, Shenzhen 518055, China, and also with Tsinghua-Berkeley Shenzhen Institute, Shenzhen 518055, China. He is now with Peng Cheng Laboratory (PCL), Shenzhen 518055, China.

M. S. Aruna Gandhi and Qian Li are with the School of Electronics and Computer Engineering, Peking University, Shenzhen 518055, China.

Shengzhen Lu and Shen Liu are with Guangdong and Hong Kong Joint Research Centre for Optical Fibre Sensors, College of Physics and Optoelectronic Engineering, Shenzhen University, Shenzhen 518060, China.

H. Y. Fu is with Tsinghua Shenzhen International Graduate School and Tsinghua-Berkeley Shenzhen Institute, Tsinghua University, Shenzhen 518055, China, and also with the Southern Marine Science and Engineering Guangdong Laboratory (Zhuhai), Zhuhai 519000, China (e-mail: hyfu@sz.tsinghua.edu.cn).

Digital Object Identifier 10.1109/JSEN.2021.3101572

tonic device research community. Fiber optic sensors, with the merits of electromagnetic immunity, fast response, excellent security and free to chemical corrosion, are intensively developed for temperature monitoring [1]–[7]. Among fiber optic temperature sensors, grating based sensors [8]–[11] and interferometer based sensors have been investigated mostly [12]–[17]. Grating based temperature sensors demonstrate good potential for remote and multipoint operation. However, compared to the fiber sensors based on functionalized materials coating or polarization maintaining fiber (PMF), the sensitivity of  $\sim 10 \text{ pm}/^\circ\text{C}$  of grating based sensors is relatively lower. For interferometer based temperature sensors, Fabry-Perot interferometer (FPI) is generally developed as sensing probes for space-limited applications [5], [12] and PMF based Sagnac interferometer (SI) achieves excellent temperature response of  $\sim 1 \text{ nm}/^\circ\text{C}$  [16], [18], [19]. Recently, sensors based on reflective Lyot filter (RLF) have been reported for different applications including temperature monitoring [4], [20], [21]. The RLF, which consists of a polarizer and a section of PMF, shows a great potential application for temperature monitoring with high sensitivity of  $-1.46 \text{ nm}/^\circ\text{C}$  [4]. As a combination of reflective transmission and good temperature response, the RLF enables the highly sensitive temperature detection in the space-limited environment. However, the temperature response of a single interferometer remains limited by the intrinsic characteristics of the optical fiber.

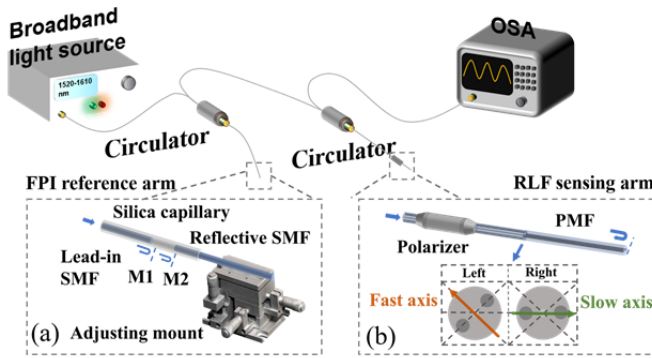


Fig. 1. Schematic of experimental setup. Inset (a) shows the schematic of the tunable extrinsic FPI, which consists of two sections of SMF and a silica capillary. The cavity length is tuned by modulating the adjusting mount. Inset (b) shows the schematic of the RLF, consisting of a polarizer and a section of PMF.

To enhance the temperature sensing performance, the functionalized materials with high thermo-optic coefficient are usually introduced with special optical fibers, such as microfiber [2], [6]. However, the pretreatment of optical fibers and packaging of functionalized materials lead to inconvenience and complexity. Vernier effect has been proved to be a good stratagem to enhance the sensing performance of interferometer based fiber optic sensors. A sensing system with Vernier effect usually consists of two interferometers. One acts as a reference arm and the other acts as a sensing arm. There is a small difference in free spectral ranges (FSRs) of two arms, working as the scales of Vernier calipers. When the peaks or dips of two arms overlap, there are peaks or dips observed in the superimposed spectrum. The FSR of superimposed spectrum is determined by the FSR difference of two arms. Generally, the spectrum of reference arm is fixed. When there is a small spectral shift in sensing arm, an explicitly huge spectral shift in superimposed spectrum of the sensing system appears. Consequently, the sensitivity can be hugely improved.

From previous works, the structures of Vernier effect based temperature sensors are cascaded SIs [22], [23], cascaded FPIs [24]–[27], cascaded Mach-Zehnder interferometers (MZIs) [28] or cascaded hybrid interferometers [29], [30]. The Lyot filter temperature sensor based on Vernier effect has been reported previously [29]. However, this work cascades the RLF with a section of hollow core fiber (HCF), the length of HCF is fixed and is difficult to control owing to the microscale of the cavity length. Based on the characteristics of Vernier effect in interferometers, it is achievable to develop the sensitivity-enhanced sensor with flexible sensitivity by control the difference of two interferometric spectra. Nevertheless, as reported, the two cascaded interferometers are fixed. The FSR of superimposed spectrum is prescribed, leading to constant sensitivity and cannot be changed afterwards. It is difficult utilizing the identical sensor for challenging application scenarios which require significant temperature sensitivities as well as different operation ranges.

In this work, we first propose a fiber temperature sensor with online controllable sensitivity based on the Vernier effect by cascading a tunable FPI and a fixed RLF. The theoretical analysis and experimental results are demonstrated. The FPI

works as the reference arm, and the FSR can be tuned freely by changing the cavity length using a 3-D adjusting mount. The adjustable FSR of FPI brings a tunable sensitivity enhancement coefficient for the cascaded structure. Combined with good temperature response of the RLF, the temperature sensor is potential to be practically applied to monitor the ambient temperature with a dynamic sensitivity range for various application scenarios, such as biomedicine, precision machining, or chemical industry, with the merits of straightforward operation and probe-type detection.

## II. PRINCIPLE AND SIMULATIONS

### A. Schematic Diagram and Principle

The schematic diagram of the proposed sensor and the experimental setup is illustrated in Fig. 1. The tunable FPI is connected with the RLF via two fiber circulators. The input light passes through the FPI and the RLF orderly, in particular experience two interferences. The schematic of FPI is shown in the Inset (a) of Fig. 1. The FPI consists of two sections of single mode fiber (SMF, G.652, YOFC) and a silica capillary. The two SMFs (lead-in SMF and reflective SMF) with an outer diameter of  $125 \mu\text{m}$  are aligned in the capillary with the inner diameter of  $127 \mu\text{m}$ . The reflective SMF is fixed on an adjusting mount, the cavity length of FPI is tuned freely by modulating the adjusting mount. There are two reflection mirrors in the FPI. One is the interface between the lead-in SMF and the air cavity, M1. The other is the interface between the air cavity and the reflective SMF, M2. The two reflective lights interfere with each other, then the interference spectrum of the FPI is obtained. It is noted that the other interface between reflective SMF and air environment is roughened to prevent additional Fresnel reflection. The FPI works as reference arm, then the reflection spectrum of reference arm  $I_{FPI}$  can be roughly expressed as [30]

$$I_{FPI} = R_1^2 + (1 - \alpha)^2(1 - R_1)^2 R_2^2 + 2(1 - \alpha)(1 - R_1)R_1 R_2 \cos \frac{4\pi n L_1}{\lambda}, \quad (1)$$

where  $R_1$  and  $R_2$  are the reflectivity coefficients of M1 and M2, respectively.  $\alpha$  is the transmission loss coefficient of the air cavity. The refractive index of the air cavity is followed as  $n = 1$ .  $L_1$  is the cavity length and  $\lambda$  is the wavelength of incident light. The FSR of the reference arm is deduced as

$$FSR_{FPI} = \frac{\lambda^2}{2nL_1}. \quad (2)$$

The schematic of the RLF is shown in the Inset (b) of Fig. 1. The output light of the FPI acts as the input light of the RLF. The light is linearly polarized by the fiber polarizer, then the pigtail fiber of polarizer is spliced with the PMF at  $45^\circ$ . The linearly polarized light is equally coupled to the slow axis and fast axis of the PMF. After a Fresnel reflection at the fiber end, the light is back to the polarizer, then the polarizer acts as a polarization analyzer. The light transmitted along the slow axis and fast axis experience an accumulated phase difference. Therefore, the two orthogonal light interfere with each other at the polarizer. After Fabry-Perot interference and birefringence interference, the output spectrum is superimposed. The RLF

acts as sensing arm, then the reflection spectrum of the sensing arm  $I_{RLF}$  can be expressed as [21]

$$I_{RLF} = \sin^2 \beta \sin^2 \gamma + \cos^2 \beta \cos^2 \gamma + \frac{1}{2} \sin 2\beta \sin 2\gamma \cos \frac{4\pi B L_2}{\lambda}, \quad (3)$$

where  $\beta = 45^\circ$ , is the angle between the polarizer and the PMF. After Fresnel reflection, the polarization state is changed to  $\gamma$  and  $L_2$  is the length of PMF.  $B = n_{slow} - n_{fast}$ , is the birefringence of PMF, to illustrate the difference of refractive indices of slow axis and fast axis.

The FSR and the dip wavelength of the interference spectrum are deduced as

$$FSR_{RLF} = \frac{\lambda^2}{2B L_2}, \quad (4)$$

$$\text{and } \lambda_m = \frac{4B L_2}{2m + 1}, \quad (5)$$

where  $m$  is an integer. Equation (5) indicates that dip wavelength is decided by the birefringence and the length of PMF simultaneously. When the RLF is exposed to environment with temperature variation, the birefringence and the length of PMF will change under the thermo-optic effect and thermo-expand effect. However, the dip wavelength shift induced by the thermo-optic effect is much larger than that induced by a thermo-expand effect. Therefore, the dip wavelength shift induced by thermo-expand effect is neglected [4]. The dependence of dip wavelength shift on ambient temperature change can be expressed as

$$\Delta \lambda_m = \lambda_m \frac{\partial B}{B \partial T} \Delta T, \quad (6)$$

where  $\partial B / \partial T$  is the thermo-optic coefficient of the PMF.

After cascading two interferometers, the transmission spectrum of the structure  $I$  can be expressed as

$$I = I_{FPI} \times I_{RLF}. \quad (7)$$

When the peak or dip of reference arm overlaps with the peak or dip of sensing arm, there is a peak or dip in the superimposed spectrum in a certain wavelength. The space between two peaks or dips, so-called FSR, of the superimposed spectrum, is determined by FSRs of reference arm and sensing arm. The FSR of superimposed spectrum is expressed as

$$FSR = \frac{FSR_{FPI} \times FSR_{RLF}}{|FSR_{FPI} - FSR_{RLF}|}. \quad (8)$$

For the sensing arm, the FSR is magnified with a coefficient  $M = FSR_{FPI} / |FSR_{FPI} - FSR_{RLF}|$ . When the sensing arm experiences a wavelength shift  $\Delta \lambda$ , then the wavelength shift of superimposed spectral envelope  $\Delta \lambda_{envelope}$  is

$$\Delta \lambda_{envelope} = M \times \Delta \lambda. \quad (9)$$

As a result, the temperature sensitivity of the sensing arm can be hugely magnified by the Vernier effect owing to the small difference between  $FSR_{FPI}$  and  $FSR_{RLF}$ . In our research, the FPI is designed as flexibly tunable. The tunable FPI leads to a tunable magnification coefficient, making the controllable sensitivity of the sensor possible.

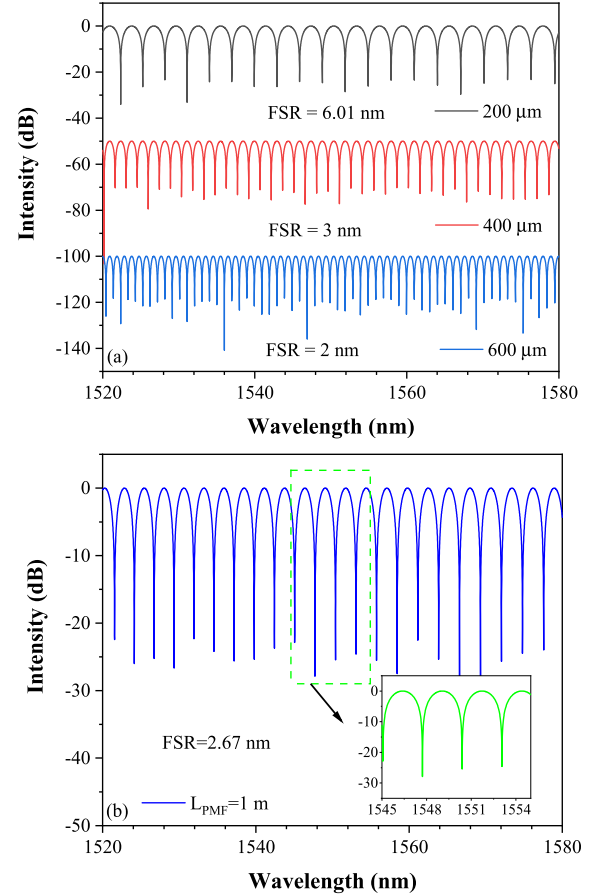


Fig. 2. (a) Simulation spectra of the FPI with the cavity length of 200  $\mu\text{m}$  (black), 400  $\mu\text{m}$  (red) and 600  $\mu\text{m}$  (blue). The corresponding FSRs are 6.01 nm, 3 nm and 2 nm, respectively. (b) Simulation spectrum of the RLF with 1-m PMF. The FSR is 2.67 nm. The inset is the magnified spectrum near 1550 nm.

## B. Simulation

First, we simulate the reflection spectra of the FPI with different cavity lengths and the RLF with 1-m PMF, the simulation results are shown in Fig. 2 (a) and (b). The calculated results show that with the increase of cavity length from 200  $\mu\text{m}$  to 600  $\mu\text{m}$  with each step of 200  $\mu\text{m}$ , FSR of the FPI near 1550 nm decreases from 6.01 nm to 2 nm. Note that the spectra are offset in the y axis to present a clear comparison of spectral characteristics, namely the y axis represents a relative intensity. The Fig. 3(a), Fig. 4(a) and Fig. 8 are processed as the same way. The simulated spectrum of the RLF with 1-m PMF (birefringence,  $B = 4.5 \times 10^{-4}$  calculated from Nufern) has an FSR of 2.67 nm near 1550 nm. We find that the FSR of the FPI with 400- $\mu\text{m}$  cavity is close to the FSR of the RLF with 1-m PMF. Next, we simulate the superimposed spectrum when cascading the 400- $\mu\text{m}$ -cavity FPI with the 1-m-PMF RLF in Fig 3.

In Fig. 3(a), the simulated spectrum of FPI with 400- $\mu\text{m}$  cavity is placed in the upper (the black curve). The simulated spectra of RLF with different birefringence are placed in the bottom (the red and blue curve). For the blue curve, the birefringence of RLF is  $4.5 \times 10^{-4}$ . For the red curve, the birefringence is  $4.498 \times 10^{-4}$  after temperature changes. When

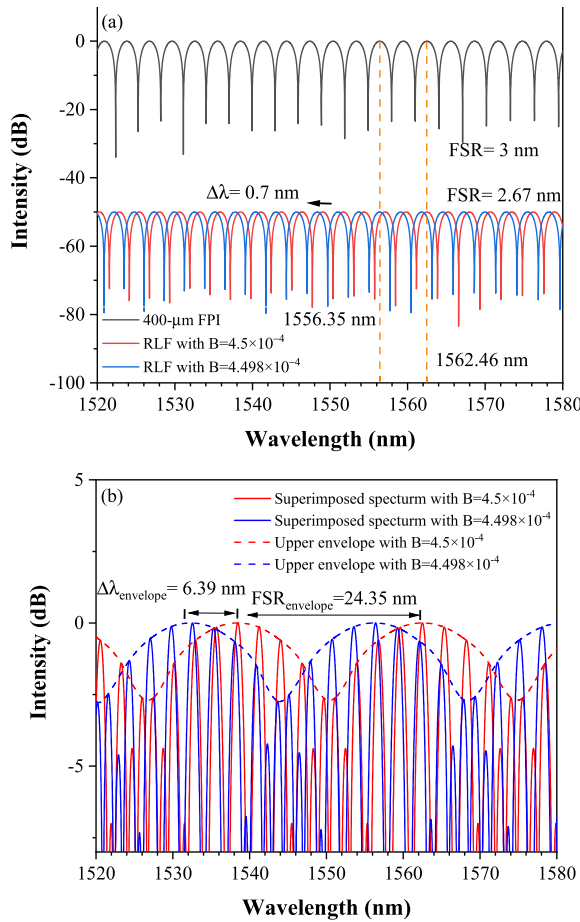


Fig. 3. (a) Simulation spectrum of FPI with 400- $\mu\text{m}$  cavity (upper) and spectral shift of RLF with different birefringence (bottom). (b) Spectral shift of superimposed spectrum envelope when cascading the 400- $\mu\text{m}$  FPI with 1-m-PMF RLF.

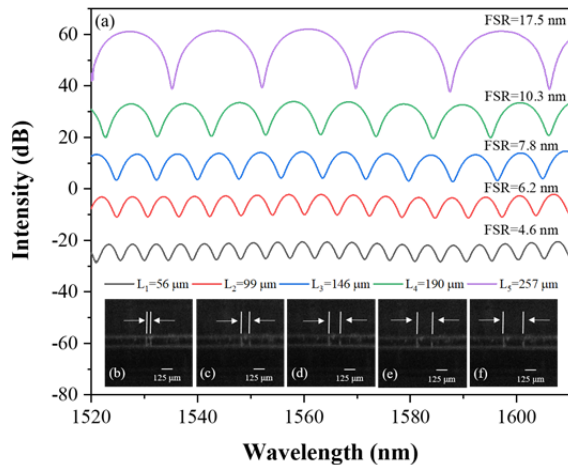


Fig. 4. (a) Measured reflection spectra of the FPI with the cavity length of 56  $\mu\text{m}$ , 99  $\mu\text{m}$ , 146  $\mu\text{m}$ , 190  $\mu\text{m}$  and 257  $\mu\text{m}$ . The corresponding microscope images of FPI with different cavity lengths are shown in (b), (c), (d), (e) and (f), respectively.

the birefringence is decreased from  $4.5 \times 10^{-4}$  to  $4.498 \times 10^{-4}$ , the dip wavelength shifts towards short wavelength by 0.7 nm. The alignment at 1562.46 nm between the two spectra of FPI and RLF shifts to 1556.35 nm. When the FPI is cascaded

with the RLF with different birefringence, the superimposed spectra are shown in Fig. 3(b). The red curve and blue curves are the superimposed spectra of the FPI and the RLF with birefringence of  $4.5 \times 10^{-4}$  and  $4.498 \times 10^{-4}$ , respectively. The corresponding dotted lines are the upper envelopes of the superimposed spectra. The FSRs of the envelopes are 24.35 nm, which is well consistent with Equation (8). When the birefringence of the RLF decreases from  $4.5 \times 10^{-4}$  to  $4.498 \times 10^{-4}$ , the envelope of superimposed spectrum blueshifts 6.39 nm. Compared to single RLF, the magnification coefficient is 9.12, which is accordant with Equation (9). Also, the peak at 1562.4 nm of the red envelope and the peak at 1556.3 nm of the blue envelope correspond to the two alignments in Fig. 3(a) at 1562.46 nm and 1556.35 nm, respectively. The simulated results clearly show that the Vernier effect enables efficient magnification of dip wavelength shift after cascading the FPI with RLF.

### III. EXPERIMENT RESULTS AND DISCUSSIONS

The experiment is carried out to investigate the temperature sensing performance of the proposed sensor with sensitivity controllability. The FPI is connected with a broadband light source (BLS, ALS-CL-15-B-FA, Amonics), and the RLF is connected with an optical spectrum analyzer (OSA, AQ6370D, Yokogawa). Fig. 4 shows the measured reflection spectra of the FPI with different cavity lengths. Note that the spectra are normalized by the reference spectrum of the light source to avoid the intensity fluctuations. All the measured spectra in this text are processed in this way.

As depicted in Fig. 4, when the cavity length is tuned from 56  $\mu\text{m}$  to 257  $\mu\text{m}$ , the FSR and fringe visibility decreases from 17.5 nm to 4.6 nm and from 22.7 dB to 6.2 dB, respectively. The change of fringe visibility results from the increase of transmission loss in the air cavity. The FSR change is caused by the different light path difference in the air cavities with varying lengths. The reflection spectrum of the RLF with 1-m-long PMF (PM1550-XP, Nufern) is described in Fig. 5. Note that the spectrum is normalized by the reference spectrum of the light source to avoid the intensity fluctuation made by the light source, and as well as other measured spectra in this manuscript. There are explicit interference patterns lie on the wavelength domain. The FSR is around 2.66 nm, and the fringe visibility is about 17.9 dB. For the cascaded structure formed by two interferometers, match of FSR determines the magnification coefficient of temperature sensitivity, and match of fringe visibility determines the envelope quality of the superimposed spectrum. In order to match the FSR of the RLF, we carefully adjust the cavity length and at the same time monitor the spectrum online on the OSA. We tune the reflective fiber to three proper positions to obtain three suitable superimposed spectra.

The superimposed spectra and the corresponding spectra of the FPI are recorded in Fig. 6. The black lines are the superimposed spectra of the cascaded structure with three different FPI states. The red curves are the sine fitting curves of the superimposed upper envelope. The sine curve is based on the maximum values of the spectral peaks. By using the sine fitting, we can get rid of the power fluctuation and track

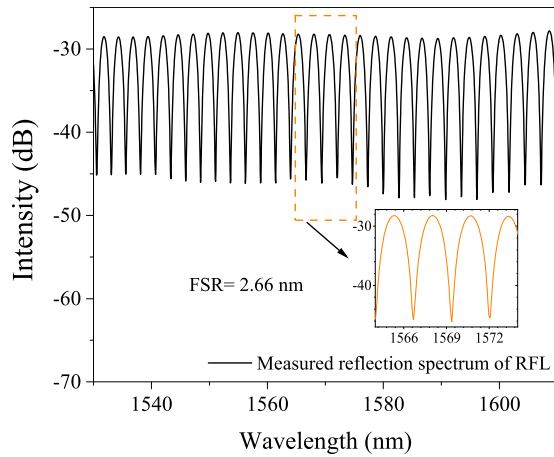


Fig. 5. Measured reflection spectrum of the RLF with 1-m long PMF. The FSR is 2.6 nm.

the precise locations of the envelope dips. The dip wavelength is determined by searching the point owns minimum intensity of each sine dip. Note that the sine fitting is in the linear form rather than the logarithmic form to well depict the upper envelope of the superimposed spectrum owing to the relatively low extinction ratio of the upper envelope. When the FSRs of the three FPIs are 3.55 nm, 3.02 nm and 2.85 nm, respectively, the extinction ratios of the three fitting curves are 3.85 dB, 3.29 dB and 2.97 dB, respectively. This is because that with the lengthening of the extrinsic FPI, the fringe visibility of FPI will be decreased. The measured FSRs of the superimposed envelopes are 10.59 nm, 21.45 nm and 38.12 nm, respectively. The measured results are basically corresponding to the Equation (8). The theoretic FSRs of the superimposed spectra are 10.61 nm, 21.45 nm and 39.9 nm. The little errors may result from the measuring error. Therefore, according to Equation (9), the temperature sensitivities of the 3 states for the sensor can be magnified by 3.98 times, 8.38 times and 15 times, respectively.

#### A. Temperature Response of Single Sensing Arm

The temperature sensing characteristics of single sensing arm is tested in the temperature range of 30 – 32 °C. The RLF is placed in a temperature controller (SNR-030H, Schneider) with the resolution of 0.1 °C, the temperature changes from 30 °C to 32 °C with each step of 0.5 °C. The spectral evolution of single RLF sensing arm is recorded. The temperature response of single RLF and the linear fitting curve are plotted in Fig. 7. In the inset, the arrow depicts the dip wavelength shift direction, the shadow represents the dip wavelength shift range.

As shown in Fig. 7, with the temperature increases from 30 °C to 32 °C, the wavelength dip shifts from 1585.33 nm to 1583.28 nm. The blue-shift results from the negative thermo-optic coefficient of PMF, which is consistent with the previous theoretical analysis. The blue-shift of each step achieves high uniformity indicating that the sensor has linear response to temperature change. The temperature sensitivity of the single RLF is  $-1.01 \text{ nm}/^\circ\text{C}$ . The sensitivity is relatively

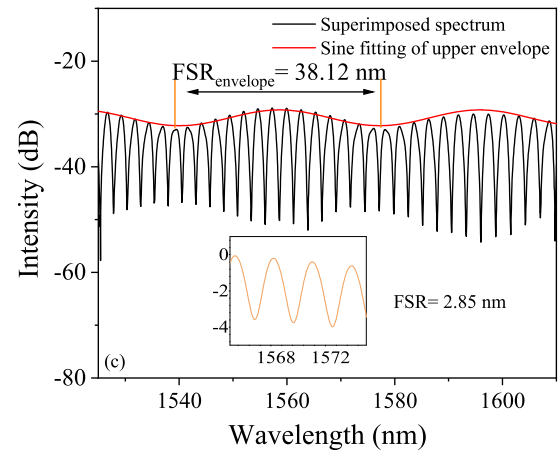
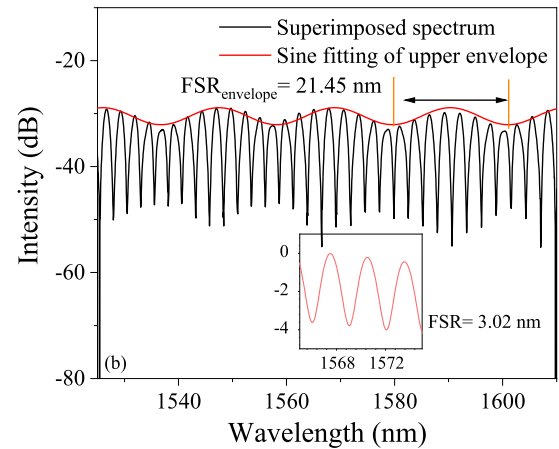
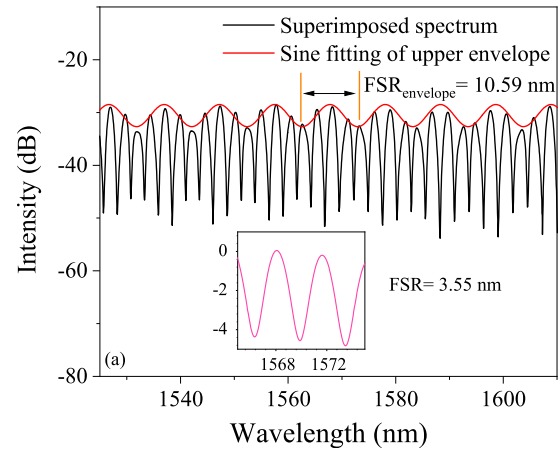


Fig. 6. Measured superimposed spectra of the cascaded sensor with the FPI FSR of (a) 3.55 nm, (b) 3.02 nm, and (c) 2.85 nm. The insets are the spectra of each FPI.

lower compared to [4]. This may result from that the PMFs offered by different manufacturers possess various birefringences and thermo-optic coefficients.

#### B. Temperature Response of Cascaded Sensing System

The temperature response of the cascaded structure with three states is tested. The experiment is carried out under the same environmental conditions of that of the single RLF sensing arm. When the FSR of the FPI is tuned to 3.55 nm,

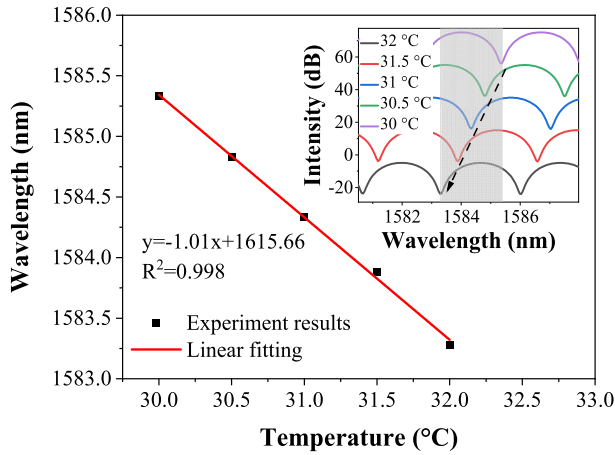


Fig. 7. Linear fitting of the temperature response of single RLF in the range of 30 – 32 °C. Inset: spectral evolution of single RLF in the temperature range of 30 – 32 °C. The arrow depicts the dip wavelength shift direction. The shadow represents the dip wavelength shift range.

3.02 nm and 2.85 nm, respectively, the corresponding temperature test results are recorded and shown in Fig 8(a), (b) and (c), respectively. Because that the FSRs of FPI and RLF are measured near 1570 nm, we track the superimposed envelope near 1570 nm to demodulate the ambient temperature change.

When the temperature is changed from 30 °C to 32 °C, the selected three envelope dips blue shift 7.8 nm, 16.68 nm and 29.47 nm, respectively. The linear fitting curves of the envelope dip wavelength shift are shown in Fig. 9. When the FSRs of the FPI are 3.55, 3.02 and 2.85, the corresponding temperature sensitivities are  $-3.82$  nm/°C,  $-8.33$  nm/°C and  $-14.63$  nm/°C, respectively. This confirms that the cascaded structure has a linear spectral response to ambient temperature changes. The sensitivity magnification coefficients are 3.78, 8.25 and 14.49, respectively. Compared to the theoretical values, the relative errors are 5%, 1.6 % and 3.4%. The little errors may result from the measurement error. It is clear that the larger FSR the superimposed envelope owns; the higher temperature sensitivity could be obtained. However, with the lengthening of the extrinsic FPI, the fringe visibility will be decreased, which causes the superimposed envelope looks flat. This will decrease the wavelength tracking precision. By using the sine fitting, the minimum value of the envelope dip can be found easily, which enables accurate temperature measurement. In the experiment, the tunable FPI is placed out of the furnace, namely the FPI is kept a constant temperature. Therefore, the tunable FPI will not affect the temperature sensing performance of the sensor. Owing to its low thermo-optic coefficient and thermo-expand coefficient, even if we put it in to the same temperature variable condition of sensor probe, the temperature response of the FPI is two orders lower than that of the PMF-based RLF, which can be ignored.

For this wavelength demodulation based fiber optic temperature sensor, the detection range is confined by the sensitivity and the wavelength window simultaneously. The relationship between the sensitivity and the temperature detection range can be expressed as a allometric function, which is shown in Figure 10.  $D_r$  is the temperature detection range of the

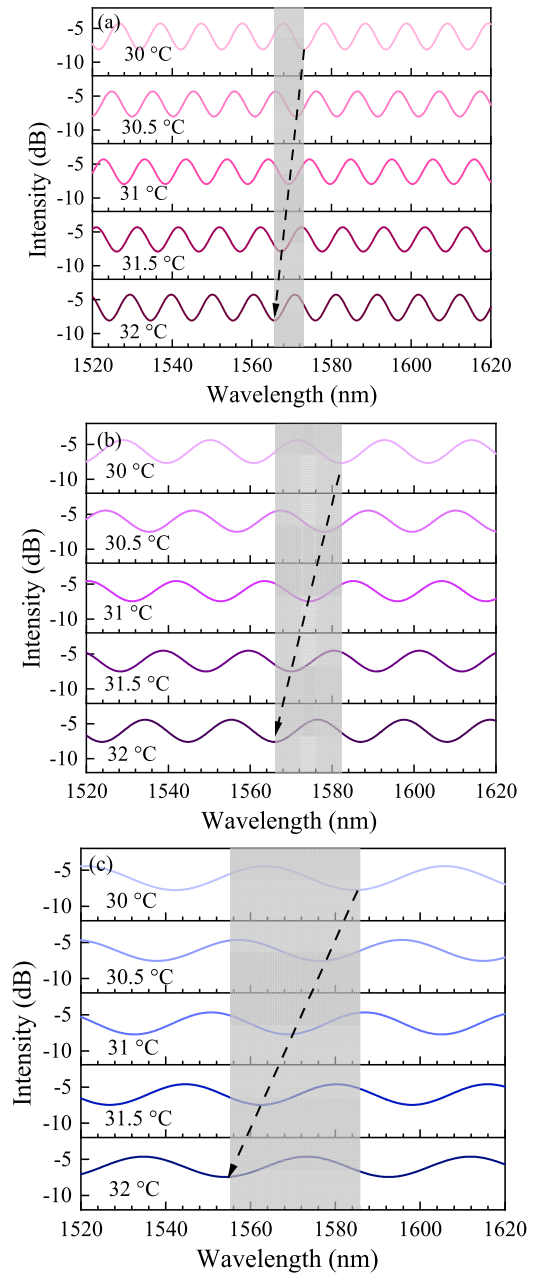


Fig. 8. Measured spectral shifts of superimposed spectra from 30 – 32 °C with the FPI FSR of (a) 3.55 nm, (b) 3.02 nm and (c) 2.85 nm. The red curves are the upper envelopes of each superimposed spectrum. The arrow depicts the dip shift direction. The shadow represents the dip wavelength shift range.

sensor, 100 is the width of the wavelength window, confined by the optical source range and OSA detection range simultaneously;  $S$  is the sensitivity of the sensor. When the temperature sensitivities are  $-3.82$  nm/°C,  $-8.33$  nm/°C and  $-14.63$  nm/°C, the corresponding temperature detection range are 26.18 °C, 12 °C and 6.84 °C, respectively. We can find that, by controlling the sensitivities of the sensor, the operation range of the sensor can be flexibly tuned. For the application scenarios required different operation ranges, we can tune the sensitivities to fulfill the maximum temperature sensitivity to realize better temperature monitoring. For the scenarios

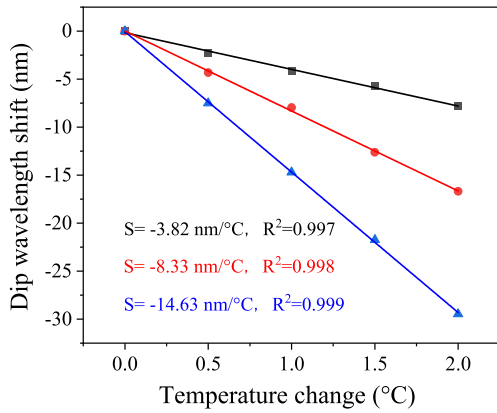


Fig. 9. Linear fitting curves of temperature sensitivities of the sensor with 3 FPI states. The envelope 1, 2 and 3 correspond to the FSR of the FPI with 3.55 nm, 3.02 nm and 2.85 nm, respectively.

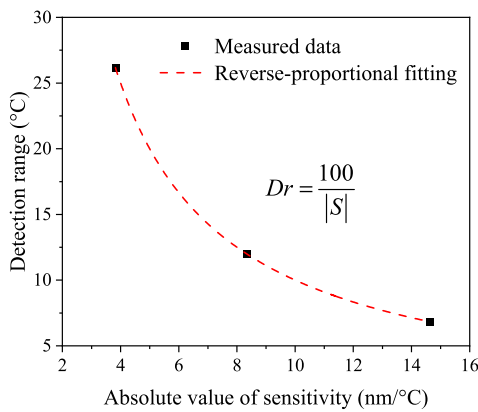


Fig. 10. Relationship between the detection range and the temperature sensitivity of the proposed sensor.

needs wide operation range, we can decrease the sensitivity by enhancing the FSR of the superimposed envelope to meet the requirement. For the scenarios needs high sensitivity, the FSR of the superimposed envelope should be decreased, with the narrower detection range. Therefore, when the sensor is applied, there is a trade-off of the sensitivity and the detection range.

We can calculate the temperature resolution using the following equation [31], [23]:

$$R_s = \frac{\delta_\lambda}{|S|}, \tag{10}$$

where the  $R_s$  is the temperature resolution of the sensor, the  $\delta_\lambda$  is the uncertainty of the fit parameter of the sine fitting, the  $|S|$  is the absolute value of the sensitivity. Note that the uncertainty value of the sine function for each state is the average uncertainty under the different temperatures. Taking the uncertainties and the three temperature sensitivities of the cascaded structure with three states of the FPI, the temperature resolutions are 0.345 °C, 0.39 °C, and 0.442 °C, respectively. The sine function is used to represent the shift of the whole upper envelope. Due to the wide range of the periodic waveform of the sine curve, the uncertainties are 1.318 nm, 3.248 nm and 6.46 nm, which are relatively high.

TABLE I  
COMPARISON BETWEEN SEVERAL TEMPERATURE SENSORS BASED ON VERNIER EFFECT

Year	Configuration	Sensitivity	Reference
2015	Cascaded SIs	-13.36 nm/°C	[22]
2017	Cascaded MZIs	0.397 nm/°C	[28]
2019	Paralleled PDMS-filled FPIs	17.75 nm/°C	[27]
2020	Cascaded SIs	-43 nm/°C	[23]
2021	Cascaded FPI and RLF	Controllable	This work

To enhance the temperature detection resolution, Gauss fitting can be used to depict the single dip [23]. For the tracked dips of the upper envelope, the uncertainties can be decreased to 0.002 nm, 0.012 nm and 0.022 nm if Gauss fitting is employed. The corresponding resolutions are 0.00057 °C, 0.0014 °C and 0.0015 °C.

In recent years, there are researches focused on temperature sensors with the Vernier effect. Here, we give a brief comparison between the proposed sensors with other representative works, as listed in Table. I. [28] cascaded two in-line MZIs, the temperature sensitivity is fixed as 0.397 nm/°C. The relatively low sensitivity is determined by the intrinsic low thermo-expand coefficient of silica. Furthermore, the MZI is fabricated by offset splicing SMFs, which enhances the fabrication complexity. In [27], the authors utilized Polydimethylsiloxane (PDMS) to enhance the temperature sensing performance, the sensor exhibited a fixed sensitivity of 17.75 nm/°C. However, the PDMS-filled FPI is difficult to manufacture, and the samples are less reproducible. Utilized the unique characteristics of PMF, cascaded SIs based on PMF were also reported in [22] and [23], the sensitivities are fixed as -13.36 nm/°C and -43 nm/°C. However, the sensors are exhibited as fiber loops, which need relatively long PMF. The PMF utilized in [22] and [23] are 3.83 m and 5.53 m, respectively. Most importantly, all the mentioned sensors have fixed sensitivities that cannot be changed. These sensors exhibit good temperature response howbeit the temperature sensitivities are constant owing to the prescribed structure and fiber lengths. Compared with them, the temperature sensor that we propose combines the advantages of extrinsic adjustable FPI and thermo-sensitive PMF, with the unique characteristics of straightforward fabrication, probe-type detection and sensitivity tunability.

#### IV. CONCLUSION

In conclusion, we theoretically propose and experimentally demonstrate a temperature sensor with online controllable sensitivity by cascading a tunable extrinsic FPI and a PMF based RLF for the first time. By controlling the FPI cavity length, the Vernier enhancement coefficient and the superimposed envelope is feasible to be tuned, which directly determines the temperature sensitivity of the sensing system. Experimental results show that our proposed sensor with different FPI cavity lengths has different temperature sensing performance, the

sensitivities of  $-3.82 \text{ nm}/^\circ\text{C}$ ,  $-8.33 \text{ nm}/^\circ\text{C}$  and  $-14.63 \text{ nm}/^\circ\text{C}$  are achieved corresponding to the three states of the FPI. Compared to the single sensing element, the sensitivities are magnified by 3.78, 8.25 and 14.49 times, respectively. Combined with the merits of straightforward fabrication, probe-type detection and online sensitivity tunability, this sensor has potential to be practically used for temperature monitoring in different application scenarios which require different sensitivities corresponding to various operation ranges.

### DISCLOSURE

The authors declare no conflict of interest.

### REFERENCES

- [1] S. M. Chandani and N. A. F. Jaeger, "Fiber-optic temperature sensor using evanescent fields in D fibers," *IEEE Photon. Technol. Lett.*, vol. 17, no. 12, pp. 2706–2708, Dec. 21, 2005.
- [2] R. Fan, Z. Mu, and J. Li, "Miniature temperature sensor based on polymer-packaged silica microfiber resonator," *J. Phys. Chem. Solids*, vol. 129, pp. 307–311, Jun. 2019.
- [3] V. L. Iezzi, S. Loranger, and R. Kashyap, "High sensitivity distributed temperature fiber sensor using stimulated Brillouin scattering," *Opt. Exp.*, vol. 25, no. 26, pp. 32591–32601, Dec. 2017.
- [4] J. Zhang *et al.*, "Highly sensitive temperature sensor using PANDA fiber Sagnac interferometer," *J. Lightw. Technol.*, vol. 29, no. 24, pp. 3640–3644, Dec. 15, 2011.
- [5] G. Liu, M. Han, and W. Hou, "High-resolution and fast-response fiber-optic temperature sensor using silicon Fabry–Perot cavity," *Opt. Exp.*, vol. 23, no. 6, pp. 7237–7247, Mar. 2015.
- [6] Z. Liu *et al.*, "PDMS-assisted microfiber M-Z interferometer with a knot resonator for temperature sensing," *IEEE Photon. Technol. Lett.*, vol. 31, no. 5, pp. 337–340, Mar. 1, 2019.
- [7] J. Zhang *et al.*, "Simultaneous measurement of refractive index and temperature using a Michelson fiber interferometer with a Hi-Bi fiber probe," *IEEE Sensors J.*, vol. 13, no. 6, pp. 2061–2065, Jun. 2013.
- [8] J. Jung, H. Nam, B. Lee, J. O. Byun, and N. S. Kim, "Fiber Bragg grating temperature sensor with controllable sensitivity," *Appl. Opt.*, vol. 38, no. 13, pp. 2752–2754, May 1999.
- [9] J. Ruan, "Fiber temperature sensor employed SMP fiber structure and a long period fiber grating based on a Sagnac loop," *Optik Int. J. Light Electron Opt.*, vol. 126, no. 24, pp. 5044–5046, Dec. 2015.
- [10] S. Sridhar, S. Sebastian, and S. Asokan, "Temperature sensor based on multi-layer MoS<sub>2</sub> coated etched fiber Bragg grating," *Appl. Opt.*, vol. 58, no. 3, pp. 535–539, Jan. 2019.
- [11] S. Zhang *et al.*, "A miniature ultra long period fiber grating for simultaneous measurement of axial strain and temperature," *Opt. Laser Technol.*, vol. 126, Jun. 2020, Art. no. 106021.
- [12] M.-Q. Chen, Y. Zhao, F. Xia, Y. Peng, and R.-J. Tong, "High sensitivity temperature sensor based on fiber air-microbubble Fabry–Perot interferometer with PDMS-filled hollow-core fiber," *Sens. Actuators A, Phys.*, vol. 275, pp. 60–66, Jun. 2018.
- [13] L.-X. Kong *et al.*, "High-sensitivity and fast-response fiber-optic micro-thermometer based on a plano-concave Fabry–Pérot cavity filled with PDMS," *Sens. Actuators A, Phys.*, vol. 281, pp. 236–242, Oct. 2018.
- [14] M. Li, Y. Liu, R. Gao, Y. Li, X. Zhao, and S. Qu, "Ultracompact fiber sensor tip based on liquid polymer-filled Fabry–Perot cavity with high temperature sensitivity," *Sens. Actuators B, Chem.*, vol. 233, pp. 496–501, Oct. 2016.
- [15] L. Shao, J. Hu, H. Lu, J. Du, T. Wu, and Y. Wang, "High-sensitivity temperature sensor based on polarization maintaining fiber Sagnac loop," *Photon. Sensors*, vol. 9, no. 1, pp. 25–32, Mar. 2019.
- [16] L. Starodumov, "Fiber Sagnac interferometer temperature sensor," *Appl. Phys. Lett.*, vol. 70, no. 1, pp. 19–21, Oct. 1997.
- [17] J. Gong *et al.*, "High sensitivity fiber temperature sensor based PDMS film on Mach–Zehnder interferometer," *Opt. Fiber Technol.*, vol. 53, Dec. 2019, Art. no. 102029.
- [18] J. Ruan, L. Hu, A. Lu, W. Lu, J. Zhu, and H. Xu, "Temperature sensor employed TCF-PMF fiber structure-based sagnac interferometer," *IEEE Photon. Technol. Lett.*, vol. 29, no. 16, pp. 1364–1366, Aug. 15, 2017.
- [19] Y. Zhao, X. Liu, R.-Q. Lv, and Q. Wang, "Simultaneous measurement of RI and temperature based on the combination of Sagnac loop mirror and balloon-like interferometer," *Sens. Actuators B, Chem.*, vol. 243, pp. 800–805, May 2017.
- [20] B. Huang and X. Shu, "Highly sensitive twist sensor based on temperature- and strain-independent fiber Lyot filter," *J. Lightw. Technol.*, vol. 35, no. 10, pp. 2026–2031, May 15, 2017.
- [21] B. Huang, X. W. Shu, and Y. Q. Du, "Intensity modulated torsion sensor based on optical fiber reflective Lyot filter," *Opt. Exp.*, vol. 25, no. 5, pp. 5081–5090, Mar. 2017.
- [22] L.-Y. Shao *et al.*, "Sensitivity-enhanced temperature sensor with cascaded fiber optic Sagnac interferometers based on Vernier-effect," *Opt. Commun.*, vol. 336, pp. 73–76, Feb. 2015.
- [23] Z. C. Ding, Z. W. Tan, P. K. Zhang, and L. W. Zhang, "Highly sensitive temperature sensor based on cascaded HiBi-FLMs with the Vernier effect," *J. Opt. Soc. Amer. B, Opt. Phys.*, vol. 37, no. 7, pp. 1948–1955, Jul. 2020.
- [24] A. D. Gomes *et al.*, "Multimode Fabry–Perot interferometer probe based on Vernier effect for enhanced temperature sensing," *Sensors*, vol. 19, no. 3, p. 453, Jan. 2019.
- [25] T. Nan *et al.*, "Ultrasensitive strain sensor based on Vernier-effect improved parallel structured fiber-optic Fabry–Perot interferometer," *Opt. Exp.*, vol. 27, no. 12, pp. 17239–17250, Jun. 2019.
- [26] J. Tian, Z. Li, Y. Sun, and Y. Yao, "High-sensitivity fiber-optic strain sensor based on the Vernier effect and separated Fabry–Perot interferometers," *J. Lightw. Technol.*, vol. 37, no. 21, pp. 5609–5618, Nov. 1, 2019.
- [27] L. Hou, C. Zhao, B. Xu, B. Mao, C. Shen, and D. N. Wang, "Highly sensitive PDMS-filled Fabry–Perot interferometer temperature sensor based on the Vernier effect," *Appl. Opt.*, vol. 58, no. 18, pp. 4858–4865, Jun. 2019.
- [28] H. Liao *et al.*, "Sensitivity amplification of fiber-optic in-line Mach–Zehnder interferometer sensors with modified Vernier-effect," *Opt. Exp.*, vol. 25, no. 22, pp. 26898–26909, Oct. 2017.
- [29] T. Ruan, L. Xia, J. Xia, and Y. Song, "Cascaded polarizer-PMF-Fabry–Pérot structure with a tunable initial state for ultra-highly sensitive temperature measurement," *Appl. Phys. Exp.*, vol. 12, no. 12, Oct. 2019, Art. no. 122002.
- [30] Y. Yang *et al.*, "Sensitivity-enhanced temperature sensor by hybrid cascaded configuration of a Sagnac loop and a F-P cavity," *Opt. Exp.*, vol. 25, no. 26, pp. 33290–33296, Dec. 2017.
- [31] Y. Zhao *et al.*, "Ultrasensitive temperature sensor with Vernier-effect improved fiber Michelson interferometer," *Opt. Exp.*, vol. 29, no. 2, pp. 1090–1101, Jan. 2021.

**Maolin Dai** (Graduate Student Member, IEEE) received the B.S. degree from Central South University in 2019. He is pursuing the M.Sc. degree in photonics with Tsinghua-Berkeley Shenzhen Institute (TBSI), Tsinghua University. His research interests include novel optical fiber devices, highly-sensitive fiber optic sensors, and fiber optics.

**Zhenmin Chen** (Member, IEEE) received the B.S. and M.Sc. degrees from Beijing Jiaotong University and the Ph.D. degree from the Department of Optical Science and Engineering, Fudan University. He is currently an Assistant Professor with Peng Cheng Laboratory (PCL). His research interests include integrated photonics, applications related to micro cavities, and fiber optic sensing technologies. He is a Life Member of The Optical Society of America (OSA).

**Yuanfang Zhao** (Graduate Student Member, IEEE) received the master's degree from Tsinghua University in 2019. She is pursuing the Ph.D. degree with Shenzhen International Graduate School and Tsinghua-Berkeley Shenzhen Institute (TBSI), Tsinghua University. Her research interests include interferometer-based optical sensors, optical Vernier effect, and high sensitivity biosensors based on LSPR/SPR.

**Xin Mu** received the B.S. degree in microelectronic engineering and the M.Sc. degree in data science and information technology from Tsinghua University, China, in 2017 and 2020, respectively. She is currently pursuing the Ph.D. degree with the University of Toronto. Her research interests include silicon photonics and optoelectronics.

**Xuanyi Liu** (Student Member, IEEE) received the B.S. degree from the College of Electronic Science and Engineering, Jilin University, Changchun, China, in 2017, the master's degree from the School of Electronic and Computer Engineering, Peking University. He is currently pursuing the Ph.D. degree with Tsinghua Shenzhen International Graduate School and Tsinghua-Berkeley Shenzhen Institute, Tsinghua University. He is a Life Member of the Optical Society of America (OSA).

**M. S. Aruna Gandhi** (Member, IEEE) was born in Manthangal Mottur, India, in 1984. She received the B.Sc. degree from Thiruvalluvar University, Tamil Nadu, India, in 2007, the M.Sc. degree in physics from Karpagam University, Coimbatore, India, in 2011, and the Ph.D. degree from VIT University, India, in 2016. After graduation, she was an Assistant Professor with Presidency University, Bengaluru, India. In 2017, she was a Postdoctoral Fellow with the School of Electronic and Computer Engineering, Peking University, Shenzhen, China, where she is currently a Research Associate. Her research interests include the design and simulation of microstructured optical devices and lab-on-a-chip-based sensors for biological applications. Dr. Aruna Gandhi is a Life Member of the Optical Society of America (OSA).

**Qian Li** (Member, IEEE) received the B.S. degree from Zhejiang University, Hangzhou, China, in 2003, the M.Sc. degree from the KTH Royal Institute of Technology, Stockholm, Sweden, in 2005, and the Ph.D. degree from Hong Kong Polytechnic University, Hong Kong, in 2009. She is an Associate Professor with the School of Electronic and Computer Engineering (ECE), Peking University. Her research interests include nonlinear optics, ultrafast optics, and integrated optics. Dr. Li is a Senior Member of the Optical Society of America (OSA).

**Shengzhen Lu** received the B.S. degree in physics from Lingnan Normal University, Zhanjiang, China, in 2019. She is currently pursuing the master's degree in optical engineering with Shenzhen University. Her major research interests focus on high-Q WGMs resonator and Fabry-Perot cavity.

**Shen Liu** received the M.S. degree in circuit and system from Chongqing University of Posts and Telecommunications in 2013 and the Ph.D. degree in optical engineering from Shenzhen University, Shenzhen, China, in 2017. He is currently an Assistant Professor with Shenzhen University. From 2017 to 2018, he was with Aston University, Birmingham, U.K., as a Postdoctoral Fellow. His current research interests focus on optical fiber sensors, WGMs resonator, and cavity optomechanics.

**H. Y. Fu** (Senior Member, IEEE) received the B.S. degree in electronic and information engineering from Zhejiang University and the M.Sc. degree in electrical engineering with a specialty in photonics from the KTH Royal Institute of Technology, Stockholm, Sweden, and the Ph.D. degree from the Department of Electrical and Electronics, Hong Kong Polytechnic University. He is currently an Associate Professor with Tsinghua-Berkeley Shenzhen Institute (TBSI), Tsinghua University. His research interests include integrated photonics and its related applications, fiber optical communications, and fiber optic sensing technologies. He is a Life Member of the Optical Society of America (OSA).